

Sympathetic cooling of the Ba^+ ion by collisions with ultracold Rb atoms: theoretical prospects

MICHał KRYCH

*Institute of Theoretical Physics, Department of Physics,
University of Warsaw, Hoża 69, 00-681 Warsaw,
Poland and Quantum Chemistry Laboratory,
Department of Chemistry, University of Warsaw,
Pasteura 1, 02-093 Warsaw, Poland*

WOJCIECH SKOMOROWSKI, FILIP PAWŁOWSKI, ROBERT MOSZYNSKI*

*Quantum Chemistry Laboratory, Department of Chemistry,
University of Warsaw, Pasteura 1, 02-093 Warsaw, Poland*

ZBIGNIEW IDZIASZEK

*Institute of Theoretical Physics, Department of Physics,
University of Warsaw, Hoża 69, 00-681 Warsaw,
Poland and Institut de Physique de Rennes,
UMR 6251 du CNRS and Université de Rennes I, 35042 Rennes Cedex, France*

* Author for correspondence; e-mail:robert.moszynski@tiger.chem.uw.edu.pl

Abstract

State-of-the-art *ab initio* techniques have been applied to compute the potential energy curves of the $(\text{BaRb})^+$ molecular ion in the Born-Oppenheimer approximation for the singlet and triplet states dissociating into the ground state ${}^1\text{S}$ Rb^+ ion and the Ba atom in the ground ${}^1\text{S}$ state, the lowest singlet or triplet D excited states, and for the singlet and triplet states dissociating into the ground state ${}^2\text{S}$ Rb atom and the ground state ${}^2\text{S}$ Ba^+ ion. The ground state potential energy was obtained with the coupled cluster method restricted to single, double, and nonperturbative triple excitations. The first triplet states in the Σ , Π , and Δ symmetries were computed with the restricted open-shell coupled cluster method restricted to single, double, and nonperturbative triple excitations. All other excited state potential energy curves were computed using the equation of motion approach within the coupled-cluster singles, doubles, and linear triples framework. The long-range coefficients describing the electrostatic, induction, and dispersion interactions at large interatomic distances are also reported. The electric transition dipole moments governing the $\text{X}{}^1\Sigma \rightarrow {}^1\Sigma$, ${}^1\Pi$ have been obtained as the first residue of the polarization propagator computed with the linear response coupled-cluster method restricted to single and double excitations. Nonadiabatic radial and angular coupling matrix elements, as well as the spin-orbit coupling matrix elements have been evaluated using the multireference configuration interaction method restricted to single and double excitations with a large active space. With these couplings, the spin-orbit coupled (relativistic) potential energy curves for the 0^+ and 1 states relevant for the running experiments have been obtained. Finally, relativistic transition moments and nonadiabatic coupling matrix elements were obtained from the nonrelativistic results and spin-orbit eigenvectors. The electronic structure input has been employed in the single channel scattering calculations of the collisional cross sections between the Ba^+ ion and Rb atom. Both nonrelativistic and relativistic potentials were used in these calculations. Our results show that the inelastic cross section corresponding to the charge transfer from the Rb atom to the Ba^+ ion is much smaller than the elastic one over a wide range of energies up to 1 mK. This suggests that sympathetic cooling of the Ba^+ ion by collisions with ultracold Rb atoms should be possible.

I. INTRODUCTION

Nowadays an increasing number of experimental groups worldwide start to work with hybrid systems involving cold or ultracold trapped atoms and ions [1–5]. Apart from the fundamental interest in the physics of atom-ion collisions in the quantum regime [6–8], these new systems are very attractive from the point of view of quantum information processing [9, 10], studying many-body effects of ion impurities [11], or creation of the molecular ions [12]. One type of ongoing experiments is focused on studying the collisional processes in cold clouds of atoms and ions, like Yb with Yb^+ and Na with Ca^+ [1, 2] stored in dual hybrid charged-neutral traps at mK temperatures. Other experiments, in contrast, study the dynamics of single ions like Ba^+ or Yb^+ trapped in RF potentials and immersed in Bose-Einstein condensates [3–5]. In such experiments the ultracold cloud of atoms is prepared using standard cooling and trapping techniques, while the ion is laser cooled separately in RF trap and later overlapped with the Bose-condensed atoms. The atom-ion collisions can lead to further sympathetic cooling of the ion, but the net cooling effect depends on the interplay of (*i*) the two-body collisional properties, (*ii*) the micromotion of the ion due to the time-dependent RF potential, (*iii*) the collective phenomena resulting from the coherent properties of the condensate additionally modified by the presence of an ionic impurity. In this paper we perform a first step towards understanding the sympathetic cooling process of Ba^+ ion with Rb atoms, by calculating highly accurate molecular potentials and determining the single channel elastic, spin-exchange and charge-transfer collision rates.

In a recent paper Makarov et al. [13] performed *ab initio* and dynamical calculations on the $(\text{CaNa})^+$ molecular ion. The results of these calculations suggest that the milliKelvin regime of collisional cooling of calcium ions by sodium atoms is very favorable, with the rate coefficient for charge transfer from the Na atom to the Ca^+ ion several orders of magnitude smaller than the rate for elastic and spin-exchange collisions. This strongly suggests that sympathetic cooling of ions by collisions with ultracold atoms should be possible. This system was further studied in the ultracold regime in Ref. [8] within the multichannel quantum defect formalism. In the present paper we investigate the possibility of sympathetic cooling for yet another system of experimental interest [5]: Ba^+ ions cooled by collisions with ultracold Rb atoms.

Theoretical modeling of collisions in the ultracold regime requires a lot of care [14–18].

First of all, the electronic states involved in the dynamics must be computed with the state-of-the-art methods of quantum chemistry. In particular, these methods should be size-consistent in order to ensure a proper dissociation of the molecular state, and must sufficiently account for the electronic correlation. Moreover, any information on the long-range asymptotics of the potentials is very important. Finally, all couplings between the molecular states, both those resulting from the spin-orbit interaction and from the nonadiabatic effects, should be considered. Having the electronic structure results at hand, exact quantum-dynamical calculations should be performed to get the cross sections and collisional rates.

In a recent series of papers Knecht et al. [19, 20] reported nonrelativistic, scalar relativistic, and fully relativistic *ab initio* potential energy curves for the $(\text{BaRb})^+$ molecular ion. Unfortunately, the approach adopted in these papers is not size-consistent, so the results at large internuclear distances may not be accurate enough. Moreover, excitations in the wave function beyond the doubles levels were included only for the simplest single reference closed-shell and high-spin states. Also, the transition moments between states, necessary to model the radiative charge transfer process from the Rb atom to the Ba^+ ion, were not computed. Finally, the nonadiabatic coupling matrix elements between different molecular states were not considered. We believe that such a level of *ab initio* calculations is not sufficient to properly model ultracold collisions in the $(\text{BaRb})^+$ molecular ion. Therefore, in the present paper we report state-of-the-art *ab initio* potential energy curves for the $(\text{BaRb})^+$ molecular ion in the Born-Oppenheimer approximation for the singlet and triplet states dissociating into the ground state ^1S Rb^+ ion and the Ba atom in the ground ^1S state, the lowest singlet or triplet D excited states, and for the singlet and triplet states dissociating into the ground state ^2S Rb atom and the ground state ^2S Ba^+ ion, electric transition dipole moments, nonadiabatic and spin-orbit coupling matrix elements. Except for the spin-orbit coupling and some nonadiabatic coupling matrix elements, all the results were obtained with size-consistent methods based on the coupled cluster ansatz including triple excitations. The nonrelativistic results are transformed to the relativistic basis, thus allowing to judge the importance of the relativistic effects, and to use our data in quantum dynamical calculations both within the Hund's case (a) and (c). Finally, we report single channel calculations of the elastic, spin-flip, and charge transfer cross sections. This will allow us to obtain the ratio of inelastic to elastic cross sections at various temperatures, and thus give a first estimate of

the efficiency of the sympathetic cooling of the barium ion by collisions ultracold rubidium atoms.

The plan of this paper is as follows. In Sec. II we introduce the theoretical models used in our calculations. We start this section with a description of the methods used in *ab initio* calculations of the Born-Oppenheimer potential energy curves and electric transition dipole moments for $(\text{BaRb})^+$. We continue with the calculations of the nonadiabatic and spin-orbit coupling matrix elements, and of the relativistic potentials. The choice of fixing the long-range coefficients at their *ab initio* values is also addressed. The remaining part of this section is devoted to the second step of the Born-Oppenheimer approximation, i.e. to dynamical calculations of the elastic, spin-flip, and charge transfer scattering cross sections. Numerical results are presented and discussed in Sec. III. We start this section with the discussion of the ground and excited states potentials. Next we turn to the nonadiabatic coupling matrix elements and electric transition dipole moments. The effects of the spin-orbit coupling on the potentials, transition moments, and nonadiabatic coupling matrix elements are also addressed. Whenever possible, our theoretical results are compared with the available *ab initio* data [19, 20]. Once the results of the electronic structure calculations are presented and discussed we turn to the problem of producing cold barium ions. We present the results for the elastic, spin-flip, and charge transfer cross sections for both the nonrelativistic and relativistic potentials, and discuss the efficiency of the sympathetic cooling leading to cold barium ions. Finally, in Sec. IV we conclude our paper.

II. COMPUTATIONAL DETAILS

A. Electronic structure calculations

When dealing with collisions at ultra-low temperatures the accuracy of the potential in the long range is very important. Therefore, the methods used in the calculations should be size-consistent in order to ensure a proper dissociation of the electronic state, and a proper long-range asymptotics of the potential. In the present paper we adopt the computational scheme successfully applied to the ground and excited states of the calcium dimer [14–18]. The potential energy curves for the ground and excited states of the $(\text{BaRb})^+$ molecular ion

have been obtained by a supermolecule method:

$$V^{2S+1|\Lambda|}(R) = E_{AB}^{SM} - E_A^{SM} - E_B^{SM} \quad (1)$$

where E_{AB}^{SM} denotes the energy of the dimer computed using the supermolecule method SM, and E_X^{SM} , $X=A$ or B , is the energy of the atom X . For the ground state potential we used the coupled cluster method restricted to single, double, and noniterative triple excitations, CCSD(T). For the first triplet states of the Σ , Π , and Δ symmetries we employed the restricted open-shell coupled cluster method restricted to single, double, and noniterative triple excitations, RCCSD(T). Calculations on all other excited states employed the linear response theory (equation of motion) within the coupled-cluster singles, doubles, and linear triples (LRCC3) framework [21, 22]. Note that the second and higher triplet states and all excited singlet states are open-shell systems that cannot be described with a single high-spin reference function, so one has to resort to methods especially designed to describe open-shell situations [23]. The CCSD(T) and LRCC3 calculations were performed with the DALTON program [24], while RCCSD(T) calculations were done with the MOLPRO suite of codes [25]. It is interesting to note at this point that even though $(\text{BaRb})^+$ is effectively a two-electron system, triple excitations are very important. A more detailed discussion of this point will be presented in sec. III. In principle we could use the LRCC3 method to obtain all the excited state potentials in any symmetry. However, the LRCC3 method is computationally more expensive than the RCCSD(T) approach, so we decided to use the latter when possible. However, we have checked for a few points that the RCCSD(T) and LRCC3 results for the $(1)^3\Sigma$, $(1)^3\Pi$, and $(1)^3\Delta$ are very close.

The long-range asymptotics of the potentials is of primary importance for cold collisions. Therefore, for each state we have computed the leading long-range coefficients describing the electrostatic, induction, and dispersion interactions. For the ground $X^1\Sigma$ state dissociating into $\text{Rb}^+(^1S) + \text{Ba}(^1S)$ and for the first excited singlet and triplet states dissociating into the $\text{Ba}^+(^2S) + \text{Rb}(^2S)$ the leading long-range asymptotics at large internuclear distances R reads:

$$V^{2S+1|\Lambda|}(R) = -\frac{C_4^{\text{ind}}}{R^4} - \frac{C_6^{\text{ind}}}{R^6} - \frac{C_6^{\text{disp}}}{R^6} + \dots, \quad (2)$$

where the long-range coefficients C_4^{ind} , C_6^{ind} , and C_6^{disp} are given by the standard expressions (see, e.g. Refs. [28, 29]) that can be derived from the multipole expansion of the interatomic interaction operator. The long-range induction and dispersion coefficients were

computed with the recently introduced explicitly connected representation of the expectation value and polarization propagator within the coupled cluster method [30, 31], and the best approximation XCCSD4 proposed by Korona and collaborators [32]. For the singlet and triplet states dissociating into $\text{Ba}^+(^2\text{S})$ ion and $\text{Rb}(^2\text{S})$ ion the induction coefficients were obtained from finite-field RCCSD(T) calculations, while the dispersion coefficient from the sum-over-state expression with the transition moments and excitation energies computed with the multireference configuration interaction method limited to single and double excitations (MRCI). Specifically, the transition moments and excitation energies of the $\text{Ba}^+(^2\text{S})$ ion were obtained in this way, while the Rb polarizability at imaginary frequency was taken from highly accurate relativistic calculations from the group of Derevianko [35].

For the molecular states of the $(\text{BaRb})^+$ ion dissociating into $\text{Ba}(^{1/3}\text{D}) + \text{Rb}^+(^1\text{S})$ the long-range asymptotics of the potentials is slightly more complicated and reads:

$$V^{2\text{S}+1|\Lambda|}(R) = \frac{C_3^{\text{elst}}}{R^3} - \frac{C_4^{\text{ind}}}{R^4} + \frac{C_5^{\text{elst}}}{R^5} - \frac{C_6^{\text{ind}}}{R^6} - \frac{C_6^{\text{disp}}}{R^6} + \dots, \quad (3)$$

where the new terms appearing in the expression above describe the long-range charge-quadrupole (C_3^{elst}) and charge-hexadecapole (C_5^{elst}) interactions. The mathematical expressions for the coefficients of Eq. (3) are given by:

$$C_3^{\text{elst}} = (-1)^{2+\Lambda} \begin{pmatrix} 2 & 2 & 2 \\ -\Lambda & 0 & \Lambda \end{pmatrix} \langle ^{1/3}\text{D} || Q_2 || ^{1/3}\text{D} \rangle, \quad (4)$$

$$C_4^{\text{ind}} = \frac{1}{2} \left(\alpha_0 + \frac{3\Lambda^2 - 6}{6} \alpha_2 \right) \quad (5)$$

$$C_5^{\text{elst}} = (-1)^{2+\Lambda} \begin{pmatrix} 2 & 4 & 2 \\ -\Lambda & 0 & \Lambda \end{pmatrix} \langle ^{1/3}\text{D} || Q_4 || ^{1/3}\text{D} \rangle, \quad (6)$$

$$C_6^{\text{ind}} = \frac{1}{2} C_{zz,zz}, \quad (7)$$

$$C_6^{\text{disp}} = \frac{1}{2\pi} \int_0^\infty \alpha_0^{\text{Rb}^+}(i\omega) \left(6\alpha_0(i\omega) + 3 \frac{3\Lambda^2 - 6}{6} \alpha_2(i\omega) \right) d\omega. \quad (8)$$

In these equations the expression in round brackets is a $3j$ symbol, $\langle ^{1/3}\text{D} || Q_l || ^{1/3}\text{D} \rangle$, ($l = 2$ or 4) denotes the reduced matrix element of the quadrupole and hexadecapole moment, respectively, α_0 and α_2 are the scalar and tensor components of the electric dipole polarizability tensor of the Ba atom in the $^{1/3}\text{D}$ state [33], while $C_{zz,zz}$ is the z component of the quadrupole polarizability of $\text{Ba}(^{1/3}\text{D})$. Finally, $\alpha_0^{\text{Rb}^+}$ is the polarizability of the rubidium ion

$\text{Rb}^+(^1\text{S})$. The electrostatic coefficients C_3^{elst} and C_5^{elst} for the Σ , Π , and Δ states are not independent, and are connected one to the other by the following relations:

$$C_3^{\text{elst}}(\Sigma) = -C_3^{\text{elst}}(\Delta) = 2C_3^{\text{elst}}(\Pi), \quad C_5^{\text{elst}}(\Sigma) = 6C_5^{\text{elst}}(\Delta) = -\frac{3}{2}C_5^{\text{elst}}(\Pi). \quad (9)$$

Note parenthetically that all coefficients that lead to attractive interactions (induction and dispersion terms) are assumed to be positive, while the electrostatic constants may result in both attractive and repulsive interactions, so they enter with their true sign. The values of the quadrupole moments, and scalar and tensor dipole polarizabilities, as well as the components of the quadrupole polarizability were obtained from finite-field LRCC3 calculations on the $^{1/3}\text{D}$ state of the atom. The hexadecapole moment of the singlet state was obtained as an excited state expectation value within the linear response CCSD formalism of Christiansen et al. [26], while for the triplet state from the MRCI calculations. The vector component of the dipole polarizability cannot be obtained from finite-field calculations, so it was obtained from the sum-over-state expression with the transition moments and excitation energies computed with the MRCI method. All calculations of the long-range coefficients employed both DALTON [24] and MOLPRO [25] suites of codes.

The transitions from the ground $\text{X}^1\Sigma$ state to the $^1\Sigma$ and $^1\Pi$ states are electric dipole allowed. The transition dipole moments for the electric, μ_i , transitions were computed from the following expression [27]:

$$\mu_i = \langle \Psi_{\text{AB}}^{\text{X}} | r_i | \Psi_{\text{AB}}^{\text{exc}} \rangle, \quad (10)$$

where r_i denotes the i th component of the position vector, while $\Psi_{\text{AB}}^{\text{X}}$ and $\Psi_{\text{AB}}^{\text{exc}}$ are the wave functions for the ground and excited states, respectively. Note that in Eq. (10) $i = x$ or y corresponds to transitions to $^1\Pi$ states, while $i = z$ corresponds to transitions to $^1\Sigma$ states. In the present calculations the electric transition dipole moments were computed as the first residue of the LRCCSD linear response function with two electric, r , operators [21]. In these calculations we have used the DALTON program [24]. We have evaluated the dependence of the transition dipole moments with the internuclear distance for the same set of distances as the excited state potential energy curves.

As will be shown in the next section the electronic states of the low lying excited states of the $(\text{BaRb})^+$ molecular ion show strong nonadiabatic couplings. Therefore, in this work we have computed the most important radial

$$R(R) = \langle (n)^{2S+1} |\Lambda| \frac{\partial}{\partial R} |(n')^{2S+1} |\Lambda| \rangle, \quad (11)$$

and angular

$$A(R) = \langle (n)^{2S+1}|\Lambda||L_+|(n')^{2S+1}|\Lambda' \rangle, \quad (12)$$

coupling matrix elements. In the above equations $\partial/\partial R$ and L_+ denote differentiation with respect to the internuclear distance and the electronic angular momentum operator, respectively. Note that the radial operator couples states of the same multiplicity and symmetry, while the electronic angular momentum operator couples states with Λ differing by one. In the present calculations the angular coupling between the singlet states was computed as the first residue of the LRCCSD linear response function with two angular momentum operators L [21]. In these calculations we have used the DALTON program [24]. All other nonadiabatic couplings were obtained with the MRCI method and the MOLPRO code [25]. We have evaluated the dependence of the nonadiabatic coupling matrix elements with the internuclear distance for the same set of distances as the excited state potential energy curves.

Barium and rubidium are heavy systems, so the electronic states of the $(\text{BaRb})^+$ molecular ion are strongly mixed by the spin-orbit (SO) interactions. Therefore, in any analysis of the collisional cross sections between Ba^+ and Rb the SO coupling and its dependence on the internuclear distance R must be taken into account. We have evaluated the spin-orbit coupling matrix elements for the lowest dimer states that couple to the 0^+ and 1 states of $(\text{BaRb})^+$, with the spin-orbit coupling operator H_{SO} defined within the Breit-Pauli approximation [36]. The spin-orbit coupling matrix elements have been computed within the MRCI framework with the MOLPRO code [25]. The full spin-orbit Hamiltonian has been used in the calculations, i.e. both the one- and two-electron spin-orbit integrals were included. Having the spin-orbit coupling matrix elements at hand, we can build up the matrices that will generate the potential energies of the spin-orbit states that couple to 0^+ and 1 symmetry.

The matrix for the 1 states writes:

$$\begin{pmatrix} V^{(1)^1\Pi} & \langle (1)^1\Pi | H_{\text{SO}} | (1)^3\Sigma \rangle & \langle (1)^1\Pi | H_{\text{SO}} | (1)^3\Delta \rangle & \langle (1)^1\Pi | H_{\text{SO}} | (2)^3\Sigma \rangle & \langle (1)^1\Pi | H_{\text{SO}} | (1)^3\Pi \rangle \\ \langle (1)^3\Sigma | H_{\text{SO}} | (1)^1\Pi \rangle & V^{(1)^3\Sigma} & 0 & 0 & \langle (1)^3\Sigma | H_{\text{SO}} | (1)^3\Pi \rangle \\ \langle (1)^3\Delta | H_{\text{SO}} | (1)^1\Pi \rangle & 0 & V^{(1)^3\Delta} - \langle (1)^3\Delta | H_{\text{SO}} | (1)^3\Delta \rangle & 0 & \langle (1)^3\Delta | H_{\text{SO}} | (1)^3\Pi \rangle \\ \langle (2)^3\Sigma | H_{\text{SO}} | (1)^1\Pi \rangle & 0 & 0 & V^{(2)^3\Sigma} & \langle (2)^3\Sigma | H_{\text{SO}} | (1)^3\Pi \rangle \\ \langle (1)^3\Pi | H_{\text{SO}} | (1)^1\Pi \rangle & \langle (1)^3\Pi | H_{\text{SO}} | (1)^3\Sigma \rangle & \langle (1)^3\Pi | H_{\text{SO}} | (1)^3\Delta \rangle & \langle (1)^3\Pi | H_{\text{SO}} | (2)^3\Sigma \rangle & V^{(1)^3\Pi} \end{pmatrix} \quad (13)$$

while the matrix for the 0^+ states is given by:

$$\begin{pmatrix} V^{(1)^3\Pi} - \langle (1)^3\Pi | H_{\text{SO}} | (1)^3\Pi \rangle & \langle (1)^3\Pi | H_{\text{SO}} | X^1\Sigma \rangle & \langle (1)^3\Pi | H_{\text{SO}} | (2)^1\Sigma \rangle & \langle (1)^3\Pi | H_{\text{SO}} | (1)^1\Sigma \rangle \\ \langle X^1\Sigma | H_{\text{SO}} | (1)^3\Pi \rangle & V^{X^1\Sigma} & 0 & 0 \\ \langle (2)^1\Sigma | H_{\text{SO}} | (1)^3\Pi \rangle & 0 & V^{(2)^1\Sigma} & 0 \\ \langle (3)^1\Sigma | H_{\text{SO}} | (1)^3\Pi \rangle & 0 & 0 & V^{(3)^1\Sigma} \end{pmatrix} \quad (14)$$

Diagonalization of these matrices gives the spin-orbit coupled potential energy curves for the 1 and 0^+ states, respectively. Note that all potentials in the matrices (13) and (14) were taken from CCSD(T), RCCSD(T), and LRCC3 calculations. Only the diagonal and nondiagonal spin-orbit coupling matrix elements were obtained with the MRCI method. Once the eigenvectors of these matrices are available, one can easily get the electric dipole transition moments and the nonadiabatic coupling matrix elements between the relativistic states.

Finally, the long-range coefficients corresponding to the relativistic potentials were obtained by diagonalizing the matrices of Eq. (13) and (14) with the potentials expanded according to Eqs. (2)–(3) and the spin-orbit coupling matrix elements fixed at the atomic values. Note that unlike in the case of resonant interactions between like atoms [43], the SO coupling does not change the leading power in the asymptotic expansion of the interaction energy, but only changes the numerical values of the coefficients. One should also note that the atomic SO coupling does not change in our model the long-range coefficients for the $(1)^1\Sigma$ and $(2)^1\Sigma$ states due to the different dissociation limits: $\text{Ba}^{(1/3)\text{D}} + \text{Rb}^{(1)\text{S}}$ versus $\text{Ba}^{+(2)\text{S}} + \text{Rb}^{(2)\text{S}}$.

In order to mimic the scalar relativistic effects some electrons were described by pseudopotentials. For Ba and Rb we took the ECP46MDF [44] and ECP28MDF [45] pseudopotentials, respectively, from the Stuttgart library. For both barium and rubidium we used the *spdfg* quality basis sets suggested in Refs. [44, 45]. The full basis of the dimer was used in the supermolecule calculations and the Boys and Bernardi scheme was used to correct for the basis-set superposition error [47].

It should be stressed at this point that the *ab initio* results reported in the present paper obtained by the *ab initio* methods described above will allow to perform dynamical calculations of the cross sections in the nonadiabatic, multichannel regime, both in the Hund's case (a) (nonrelativistic states, SO and nonadiabatic couplings, and transition moments) and (c)

(relativistic potentials, nonadiabatic couplings, and transition moments), cf. Ref. [46].

Finally, to conclude this section we would like to emphasize that almost all *ab initio* results were obtained with the most advanced size-consistent methods of quantum chemistry: CCSD(T), RCCSD(T), and LRCC3. Only the SO coupling matrix elements and nonadiabatic matrix elements were obtained with the MRCI method which is not size consistent. Fortunately enough, all of the couplings are important in the region of the curve crossings or avoided crossings and vanish at large distances, so the effect of the size-inconsistency of MRCI on our results should not be dramatic.

B. Dynamical calculations

In collisions of the $\text{Ba}^+(^2\text{S})$ ion with $\text{Rb}(^2\text{S})$ atom we have basically three types of processes: elastic scattering in the singlet and triplet potentials, spin-flip (spin-exchange) process, and the inelastic radiative charge transfer from the singlet and triplet manifolds of Ba^+Rb to the ground state of BaRb^+ . In the present paper we restrict ourselves to single channel calculations. A more detailed multichannel treatment will be presented elsewhere.

To compute the elastic cross sections we need to solve the radial Schrödinger equation for the relative motion of the Ba^+ ion and Rb atom at an energy E :

$$\left(\frac{d^2}{dR^2} - \frac{2\mu}{\hbar^2} V(R) - \frac{J(J+1)}{R^2} + \frac{2\mu E}{\hbar^2} \right) \Psi_{EJ}(R) = 0, \quad (15)$$

subject to the following normalization conditions:

$$\int_0^\infty \Psi_{E_1 J}^*(R) \Psi_{E_2 J}(R) dR = \delta(E_1 - E_2), \quad (16)$$

where $\Psi_{EJ}(R)$ is the scattering wave function, μ is the reduced mass of the $(\text{BaRb})^+$ ion, and $V(R)$ stands for the interaction potential of $\text{Ba}^+(^2\text{S})$ with $\text{Rb}(^2\text{S})$ in the singlet or triplet manifold. Note that the normalization condition of Eq. (16) is equivalent to the following large- R behavior of the wave function $\Psi_{EJ}(R)$,

$$\Psi_{EJ}(R) \sim \left(\frac{2\mu}{\pi\hbar^2 k} \right)^{1/2} \sin \left(kR - \frac{J\pi}{2} + \delta_J(E) \right), \quad (17)$$

where $\delta_J(E)$ denote the phase shift corresponding to the J partial wave, and the wave vector k is given by the standard expression, $E = \frac{\hbar^2 k^2}{2\mu}$. Equation (15) subject to the normalization

condition (16) allows us to compute the cross sections for the elastic and spin-flip collisions from the standard expressions:

$$\sigma_{\text{el}}^s(E) = \frac{4\pi}{k^2} \sum_{J=0}^{\infty} (2J+1) \sin^2 \delta_J^s(E), \quad \sigma_{\text{el}}^t(E) = \frac{4\pi}{k^2} \sum_{J=0}^{\infty} (2J+1) \sin^2 \delta_J^t(E), \quad (18)$$

$$\sigma_{\text{sf}}(E) = \frac{4\pi}{k^2} \sum_{J=0}^{\infty} (2J+1) \sin^2 (\delta_J^{\text{s}}(E) - \delta_J^{\text{t}}(E)), \quad (19)$$

where the superscripts “s” and “t” on σ_{el} and δ_J pertain to the singlet and triplet potentials, respectively. Note that an exact description of the spin-flip process would require at least two coupled channels, so the expression (19) is only approximate [37]. It is derived under assumption that the hyperfine splittings are much smaller than the collision energy. However, it was shown to work relatively well, even at low energies [38, 39].

Theoretical description of the charge transfer process between the atom and the ion is somewhat more elaborate. To the first-order of perturbation theory the radiative charge transfer can be described by the following Fermi golden type expression [40]:

$$\sigma_{\text{ct}}(E) = \frac{4\pi^2\hbar}{k^2} A(E), \quad (20)$$

where the Einstein coefficient $A(E)$ is given by:

$$\begin{aligned}
A(E) &= \frac{4\alpha^3}{3e^4\hbar^2} \sum_{J'=0}^{\infty} \sum_{J''=J'\pm 1} (2J'+1) \left[\int_0^{\infty} \varepsilon^3 H_{J'} |\langle \Psi_{E'J'} | \mu(R) | \Psi_{E''J''} \rangle|^2 d\varepsilon \right. \\
&\quad \left. + \sum_{v''} H_{J'} (E_{v''J''} - E')^3 |\langle \Psi_{E'J'} | \mu(R) | \Psi_{v''J''} \rangle|^2 \right], \tag{21}
\end{aligned}$$

where the primed and double primed quantities pertain to the excited and ground state potentials, respectively, $\mu(R)$ is the transition moment from the ground to the excited electronic state, $\alpha = 1/137.035999679(94)$ is the fine structure constant, e is the electron charge, and the H  hn-London factor $H_{J'}$ is equal to $(J'+1)/(2J'+1)$ for the P branch ($J' = J'' - 1$), and to $J'/(2J'+1)$ for the R branch ($J' = J'' + 1$). Here, ε stands for the energy difference

$$\varepsilon = E'' - E' + \Delta_{\text{IP}}, \quad (22)$$

where Δ_{IP} is the difference of the ionization potentials. The scattering wave functions appearing in the expression (21) are solutions of Eq. (15), while the bound-state wave functions fulfill the following Schrödinger equation:

$$\left(\frac{d^2}{dR^2} - \frac{2\mu}{\hbar^2} V(R) - \frac{J''(J''+1)}{R^2} + \frac{2\mu E_{v''J''}}{\hbar^2} \right) \Psi_{v''J''}(R) = 0, \quad (23)$$

subject to the following normalization conditions:

$$\int_0^\infty \Psi_{v_1 J}^*(R) \Psi_{v_2 J}(R) dR = \delta_{v_1 v_2}, \quad (24)$$

where $V(R)$ stands for the ground state potential of the $(\text{BaRb})^+$ molecular ion.

A significantly simpler approach proposed in Ref. [41] approximates the sum over all continuum and bound states in Eq. (21) with a simple average of a space-varying Einstein coefficient over the initial scattering wave function $\Psi_{E' J'}$:

$$A(E) = \sum_{J'=0}^{\infty} (2J' + 1) \langle \Psi_{E' J'} | \bar{A}(R) | \Psi_{E' J'} \rangle, \quad (25)$$

where

$$\bar{A}(R) = \frac{\alpha^3}{3\hbar e^6} (\delta V)^3(R) \mu^2(R), \quad (26)$$

and $\delta V(R)$ is the difference between the excited and ground state potentials.

III. NUMERICAL RESULTS AND DISCUSSION

A. Nonrelativistic potential energy curves and spectroscopic characteristics of the ground and excited states

Calculations were done for the ground state and first eight (four singlet and four triplet) excited states of $(\text{BaRb})^+$. Two states dissociate into $\text{Ba}^+(^2\text{S}) + \text{Rb}(^2\text{S})$, three states into $\text{Ba}(^3\text{D}) + \text{Rb}^+(^1\text{S})$, and three states into $\text{Ba}(^1\text{D}) + \text{Rb}^+(^1\text{S})$. The potential energies were calculated for twenty interatomic distances R ranging from 4 to 50 bohr for each potential curve. The potential curves are plotted in Fig. 1, while the spectroscopic characteristics of these states are reported in Table I. The ground state is absent on figures due to its regular behaviour and single minimum, and in order to increase the visibility of the other states. The separated atoms energy for each state was set equal to the experimental value. Numerical values of the potentials are available from the authors on request.

Before going on with the discussion of the potentials let us note that the atomic excitation energies obtained from the LRCC3 calculations are very accurate. Our predicted position of the nonrelativistic ^3D state of barium is 9422 cm^{-1} , to be compared with the experimental value of 9357 cm^{-1} [42] deduced from the positions of the states in the D multiplet and the Landé rule. For the ^1D state of Ba we obtain 11907 cm^{-1} , in a relatively good agreement

with the experimental value of 11395 cm^{-1} [42]. It is worth noting that the present results for the atomic excitation energies are as accurate as the results of fully relativistic atomic calculations of Kozlov and Porsev [52], and more accurate than the data obtained from fully relativistic Dirac-Coulomb calculations [20]. To further assess the quality of the methods, basis-sets and pseudopotentials employed in the present paper we have computed the static polarizabilities of the ground state of Ba atom, of the ground state of the Ba^+ ion, and the scalar and tensor components of the polarizability of $\text{Ba}(^1\text{D})$. The present polarizability of the ground state of the barium atom is 272.5 a.u. The experimental value is 268 ± 22 [48], while the best theoretical result of Kozlov and Porsev [52] is 264 a.u.. Also the static polarizability of the Ba^+ ion, 132 a.u., is in a fairly good agreement with the result of fully relativistic calculations of Ref. [49], 124.15 a.u., of Ref. [50], 124.26 a.u., and with the most recent experimental result, 123.88(5) a.u. [51]. For the ^1D state we get the scalar and tensor polarizabilities of 289 and 73 a.u., in a fair agreement with the results of Ref. [52], 266 and 81 a.u., respectively. The methods employed in the present paper do not allow for a consistent calculation of the dissociation limit Δ_{IP} of the $(2)^1\Sigma$ and $(1)^3\Sigma$ states corresponding to $\text{Ba}^+(^2\text{S}) + \text{Rb}(^2\text{S})$ separated atoms, since the ground state calculations employed CCSD(T) and the calculations on the singlet and triplet excited states the LRCC3 and RCCSD(T) methods, respectively. However, we can estimate Δ_{IP} from the energy of the $(2)^1\Sigma$ and $(1)^3\Sigma$ at $R = 50$ bohr. Both the LRCC3 calculation on the singlet state and RCCSD(T) calculation on the triplet state give $\Delta_{\text{IP}} = 8097\text{ cm}^{-1}$ in a good agreement with the experimental value of 8344 cm^{-1} [42]. The fully relativistic result of Ref. [20], 8065 cm^{-1} , is very close to our value.

The ground $\text{X}^1\Sigma$ state of the $(\text{BaRb})^+$ molecular ion is a strongly bound state with the binding energy of 5136 cm^{-1} . The minimum on the potential energy curve for this state appears at a relatively large distance $R_e = 8.67$ bohr. The origins of the binding can be explained by using the symmetry-adapted perturbation theory of intermolecular forces (SAPT) [28, 29]. As could be guessed, the interaction energy at the minimum results from a subtle balance of the induction attraction and exchange-repulsion. The induction energy is huge, -14499 cm^{-1} , but is strongly quenched by the exchange-repulsion term, 10068 cm^{-1} . The electrostatic contribution due to the charge overlap of the unperturbed electron clouds of Ba and Rb^+ , -554 cm^{-1} , and dispersion term, -598 cm^{-1} is of minor importance, again in agreement with our intuition.

An inspection of Fig. 1 shows that the potential energy curves for the excited states of the $(\text{BaRb})^+$ molecular ion are smooth with well defined minima. The potential energy curves of the $(2)^1\Sigma$ and $(3)^1\Sigma$ show an avoided crossing. The potential energy curves of the $(2)^1\Sigma$ and $(2)^3\Sigma$ states exhibit a double minimum structure. The double minimum on the potential energy curve of the $(2)^1\Sigma$ state is due to the interaction with $(3)^1\Sigma$ state. Other double minimum structure can be explained from the long-range theory and will be discussed below. Some potential energy curves show maxima. These are due to the first-order electrostatic interactions in the long range, and will also be discussed in more details in sec. III B. Except for the shallow double minima structure of the $(2)^1\Sigma$ and $(2)^3\Sigma$ states, and a shallow $(3)^1\Sigma$ state, all other excited states of the $(\text{BaRb})^+$ molecular ion are strongly bound with binding energies D_e ranging from approximately 4380 cm^{-1} for the $(1)^3\Delta$ state up to 6301 cm^{-1} for the $(1)^3\Pi$ state. The $(2)^1\Sigma$ state, important from the experimental point of view, has two minima at $R_e = 9.02$ and 15.19 bohr. The depths of these minima are 911 and 576 cm^{-1} , while the barrier separating them is of 30 cm^{-1} suggesting that the tunneling between the two wells will be very fast. The $(2)^3\Sigma$ state also shows two minima at $R_e = 9.82$ and 16.78 bohr of 1874 and 697 cm^{-1} , respectively, separated by a barrier of 681 cm^{-1} .

Before comparing our results with the *ab initio* data reported in Refs. [19, 20] let us stress the importance of the triple excitations in the wave functions for some states. This point is illustrated in Fig. 2, where LRCCSD versus LRCC3 and CCSD versus CCSD(T) potential energy curves are plotted for selected states. An inspection of these figures shows that the contribution of the triple excitations is important for the excited $(2)^1\Sigma$ and $(2)^3\Sigma$ states, and relatively unimportant for the $(1)^3\Delta$ and for the $(1)^3\Pi$ states. Not shown on these figures are the $(1)^3\Sigma$, $(1)^1\Pi$, and $(1)^1\Delta$ states. For these states we find that the potential for the $(1)^3\Sigma$ state is relatively unaffected by the triple excitations, while the two other potential energy curves show large differences depending whether the T_3 cluster operator is included or not in the wave functions. These results strongly suggest that the CCSD or LRCCSD method works for those states that can be described by a single reference determinant. For open-shell states, i.e. all singlet states and the $(2)^3\Sigma$ state, the effect of the triple excitations is large and changes both the well depths and the barriers. In principle, the differences could be due to CCSD(T) vs. LRCC3 methods used in the calculations. However, as we already stated in sec. II, we have checked for a few points that the RCCSD(T) and LRCC3

results for the $(1)^3\Sigma$, $(1)^3\Pi$, and $(1)^3\Delta$ are very close. To get a better understanding of the importance of the triple excitations we analysed the energy gaps between the lowest electron configuration for a given state and the lowest triply excited configuration. It turned out that for the effectively high-spin states this energy difference was high, while for the manifestly states the opposite was true. Using simple perturbation theory arguments one can deduce that the correlation due to the triple excitations will be important for states with a small energy gap between the lowest and triply excited configurations, and much less important for states with large energy difference.

Let us compare our results with other available *ab initio* data [19]. The spectroscopic constants are listed in Table I and compared with the results of Ref. [19]. Unfortunately, Knecht et al. [19] did not report the binding energies D_e of the molecular states, but only the values of the electronic term values T_e taking the minimum of the ground state as zero of energy. An inspection of Table I shows that the agreement with the data of Knecht et al. [19] is relatively good, given the fact that their results were obtained using the internally contracted multireference configuration singles and doubles method based on a CASSCF reference function. For most of the states the computed electronic terms agree within a few hundred cm^{-1} . For the high-spin states the differences in the positions of the minima are 0.1 bohr at worst, while the electronic terms differ by 300 to 600 cm^{-1} . For the open-shell states, where the triple excitations in the wave function are important, the differences in the positions and well depths are more important. The most striking difference between the present results and the data of Ref. [19] is the $(1)^1\Pi$ state. Here, the difference in the position of the minimum is 0.6 bohr, and the difference in T_e is as much as 3300 cm^{-1} . The double minimum structure of the $(2)^1\Sigma$ and $(2)^3\Sigma$ states was not reproduced by MRCI calculations, but the barriers and the avoided crossing between the $(2)^1\Sigma$ and $(3)^1\Sigma$ states are reproduced. In general, the agreement is only qualitative. To end this paragraph we would like to say that the results of fully relativistic Dirac-Coulomb calculations published by the same Authors in Ref. [20] are in a much better agreement with the present data, cf. sec. III C.

B. Nonadiabatic coupling matrix elements and electric transition dipole moments from the ground $X^1\Sigma$ state

The most important nonadiabatic coupling matrix elements between the excited states of the $(\text{BaRb})^+$ molecular ion are reported on Fig. 3. The regions where these couplings could possibly be important are indicated on Fig. 1. The left pannel on this figure shows the radial coupling between the $(2)^1\Sigma$ and $(3)^1\Sigma$ states. The potential energy curves for these states reveal an avoided crossing shown on Fig. 1 at $R \approx 12$ bohr. An inspection of Fig. 3 shows that the maximum of the radial coupling between these two states corresponds to this distance. In general, the radial coupling as a function of the distance R is small, and rather localized around the point of the avoided crossing. The angular coupling matrix elements reported on the right pannel of Fig. 4 show more variations with R . The angular coupling between the $(1)^1\Pi$ and $(2)^1\Sigma$ states has a broad maximum around $R \approx 11$ bohr, and this distance roughly corresponds to the crossing of the $(1)^1\Pi$ and $(2)^1\Sigma$ potential energy curves. The angular coupling between the $(1)^3\Pi$ and $(1)^3\Sigma$ states shows a broad minimum at $R \approx 7$ bohr, and again this distance roughly corresponds to the crossing of the $(1)^3\Pi$ and $(1)^3\Sigma$ potential energy curves. The last angular coupling that may influence the dynamics of the $(\text{BaRb})^+$ molecular ion corresponds to the $(2)^3\Sigma$ and $(1)^3\Pi$ states. Here, the R dependence of the angular coupling is quite different, but the largest variations correspond again to the point, where the two curves cross, $R \approx 12$ bohr. Note parenthetically that radial coupling tends to zero as R^{-7} , the angular couplings between the $(2)^3\Sigma$ and $(1)^3\Pi$ states tends to a constant value, $\langle ^3D(M_L = 1) | L_+ | ^3D(M_L = 0) \rangle = \sqrt{3}$, while the coupling between the $(1)^1\Pi$ and $(2)^1\Sigma$ decays exponentially at large R . This unusual exponential decay is due to the different dissociation limits of the ground $X^1\Sigma$ and excited $(2)^1\Sigma$ states: $\text{Ba}^1\text{S} + \text{Rb}^1\text{S}$ versus $\text{Ba}^2\text{S} + \text{Rb}^2\text{S}$. It is gratifying to note that the MRCI method used in the calculations of the radial coupling and angular couplings between the triplet states quite precisely located the regions of the avoided crossing and curve crossing despite the fact the latter were determined from the RCCSD(T) and LRCC3 calculations. This suggests that the computed nonadiabatic coupling matrix elements are reliable, at least around of the crossings.

The electric dipole transition moments between the ground state and the three excited electric dipole-allowed states, two $^1\Sigma$ and one $^1\Pi$, are plotted in Fig. 4 as functions of the

interatomic distance R . The calculated electric transition moments show a strong dependence on the internuclear distance R . For the transition moments to the excited states of the Σ symmetry the curves show broad maxima around the positions of the depths on the potential energy curves. The transition moment to the Π state is very small, suggesting that this state will be of minor importance in the dynamics of the $(\text{BaRb})^+$ ion. At large interatomic distances the transition moments to the $(3)^1\Sigma$ and $(1)^1\Pi$ states tend to zero as $\mu_4 R^{-4}$, while the transition moment to the $(2)^1\Sigma$ state decays exponentially with the internuclear distance R . This R^{-4} dependence can be derived from the multipole expansion of the wave functions of the $(3)^1\Sigma$, $(1)^1\Pi$, and $X^1\Sigma$ states. The expressions for the leading long-range coefficient μ_4 of the electric transition dipole moments read:

$$\mu_4 = A_{|\Lambda|} \alpha_0^{\text{Rb}^+} \langle ^1\text{S} || Q_2 || ^1\text{D} \rangle, \quad (27)$$

where $A_0 = 3/2\sqrt{5}$ and $A_1 = A_0/\sqrt{3}$.

C. Spin-orbit coupling and relativistic potential energy curves, nonadiabatic coupling, and electric transition dipole moments

A large number of spin-orbit interactions couple the dimer states of the $(\text{BaRb})^+$ molecular ion. In Fig. 5 we report the R dependence of the spin-orbit coupling matrix elements that couple to the 1 and 0^+ states. These states are most interesting for the collisional dynamics of $(\text{BaRb})^+$. Similar results can easily be obtained for the 0^- , 2 , and 3 states. An inspection of Fig. 5 shows that the SO coupling matrix elements have relatively large variations at small internuclear distances and tend to zero or to the atomic values at large R . All diagonal matrix elements of the spin-orbit Hamiltonian are lower than the atomic 1^3D spin-orbit constant of barium ($\approx 150 \text{ cm}^{-1}$), while the largest nondiagonal couplings are observed for the pairs of states associated with the crossing of the corresponding potential energy curves. The accuracy of the atomic SO couplings can be judged by comparison of the computed and observed positions of the energy levels in the ^3D multiplet. The calculated energies of the $^3\text{D}_1$, $^3\text{D}_2$, and $^3\text{D}_3$ states are 9035 , 9254 , and 9680 cm^{-1} , and are in a very good agreement with the experimental values of 9034 , 9216 , and 9597 cm^{-1} [42]. It is worth noting that some of the couplings vanish at large distances due to the different dissociation limits: $\text{Ba} + \text{Rb}^+$ versus $\text{Ba}^+ + \text{Rb}$. This means that the neglect of the R dependence

of the spin-orbit matrix elements would lead to wrong relativistic potentials since some of important couplings would be neglected. As an example we can cite the coupling of the $(1)^3\Sigma$ and $(1)^3\Pi$ states. The asymptotic value is zero due to the different dissociation limits of these states: $\text{Ba}^3\text{D} + \text{Rb}^+(1\text{S})$ versus $\text{Ba}^+(2\text{S}) + \text{Rb}^2\text{S}$. Therefore, when approximating in Eq. (13) all SO couplings by the corresponding atomic values one would obtain a completely wrong matrix of the spin-orbit Hamiltonian for the 1 states since in the atomic limit $\langle (1)^3\Sigma | H_{\text{SO}} | (1)^3\Pi \rangle = 0$. In particular, in the atomic approximation the $(1)^3\Sigma$ state would remain unchanged, and as it will be shown below it changes quite a lot at small internuclear distances. The same is true for the $(2)^1\Sigma$ state.

The diagonalization of the spin-orbit Hamiltonian matrices, Eqs. (13) and (14), gives the potential energy curves of the states that couple to 1 or 0^+ symmetry. The corresponding curves for the 0^+ and 1 symmetries are reported on Fig. 6. An inspection of Figs. 1 and 6 shows that the crossings of the diabatic (nonrelativistic) states are transformed into avoided crossings on the spin-orbit coupled relativistic curves. Obviously, the inclusion of the spin-orbit interaction results in different dissociation pathways. Due to the presence of many closely located molecular states in the $^3\text{D} - ^1\text{D}$ energy range that couple to the 0^+ and 1 symmetries, the effect of the spin-orbit coupling is very pronounced. Indeed, comparison of Fig. 1 and Fig. 6 shows that the behavior of some relativistic curves is drastically modified compared to the nonrelativistic case.

In Table II we report the spectroscopic constants of the relativistic states and compare them with the available *ab initio* data of Ref. [20]. An inspection of this Table shows that the agreement between the present results and the data of Ref. [20] is excellent for the dissociations $\text{Ba}^1\text{S}_0 + \text{Rb}^+(1\text{S}_0)$ and $\text{Ba}^+(2\text{S}_{1/2}) + \text{Rb}^2\text{S}_{1/2}$. Indeed, our result for the well depth of the ground state overestimates the data of Ref. [20] by only 1.6%. For the first excited states of 0^+ and 1 symmetry, our results underestimate the values of Knecht et al. [20] by 3.1% and 3.7%, respectively. For all states mentioned above, the positions of the minima in the two calculations agree within 0.1 bohr or better. It is gratifying to observe such an excellent agreement between two different sets of *ab initio* calculations performed with different methods, CCSD(T) and RCCSD(T) in the present work vs. MRCI in Ref. [20]. Such a good agreement was expected from the analysis of the nonrelativistic results, since the triple excitations are relatively unimportant for these states. It is also worth noting that the pseudopotentials and basis sets used in our calculations [44, 45] do a very good job,

as compared to the fully relativistic Dirac-Coulomb calculations [20]. The comparison for higher excited states is less favorable. For the (3)1 state the agreement of D_e is within 4%, and R_e is shifted by 0.1 bohr. This good agreement is again not fortuitous, since the (3)1 relativistic state is dominated by the nonrelativistic (1) $^3\Delta$ component, and the latter is a high-spin state not very sensitive to triple excitations in the wave function. For other states the differences in the well depths are of the order of 8% to 13%, and mostly reflect the lack of triple excitations in the calculations of Ref. [20]. We would like to stress, however, that the overall pictures of the relativistic states in the present paper and in Ref. [20] agree quite well.

As in the nonrelativistic case, in the relativistic picture states of the same symmetry do not cross, while states of different symmetries can cross. Given the complicated pattern of the molecular states, cf. Fig. 6, the knowledge of the nonadiabatic couplings is essential for the multichannel dynamics. The nonadiabatic couplings between the relativistic states as functions of the internuclear distance R are presented on the left pannel of Fig. 7. An inspection of this figure shows that some couplings are rather localized in space with sharp maxima or minima, and some other show broad structure. All this can be rationalized by looking at the predominant singlet or triplet character of the states involved. Since all these structures can be explained in such a way, we take the coupling $\langle(5)1|L_+|(3)0^+\rangle$ as an example. The (5)1 and (3)0 $^+$ show crossing around $R \approx 12$ bohr, and in this region the nonadiabatic coupling has a broad maximum. At these distances both states are primarily singlets with only a small admixture of some triplet states. At $R \approx 15$ bohr the (3)0 $^+$ state shows an avoided crossing with the (2)0 $^+$ state. In the nonrelativistic picture the (2)0 $^+$ state is mostly dominated by the (1) $^3\Pi$ state, while the (3)0 $^+$ state by the (2) $^1\Sigma$ state. Thus, at distances larger than the avoided crossing the matrix element of L_+ between the (1) $^3\Pi$ and (1) $^1\Pi$ states is zero.

In the relativistic case many transitions that were forbidden at the nonrelativistic level due to the different multiplicities of the states involved become allowed due to admixtures of singlets to triplet and vice versa, cf. the right pannel of Fig. 7. These additional transition moments are very small, showing that the relativistic states obtained by admixture of the singlet states to triplets are almost pure triplet states. The transition moment $\langle(1)0^+|z|(4)0^+\rangle$ resembles very much $\langle(1)1\Sigma|z|(3)1\Sigma\rangle$, with little differences only at small internuclear distances. More interesting are the transition moments $\langle(1)0^+|z|(2)0^+\rangle$ and $\langle(1)0^+|z|(3)0^+\rangle$. If

one would take the sum of these two curves, the resulting curve would strongly resemble the graph for $\langle (1)^1\Sigma | z | (2)^1\Sigma \rangle$ transition moment, cf. Fig. 4. The explanation of this fact is very simple. At distances smaller than $R \approx 15$ bohr the $(3)0^+$ is predominantly a singlet state, while $(4)0^+$ has mostly triplet character. The situation is opposite at R larger than 15 bohr. This explains why we get two curves with a sharp decay to zero around 15 bohr.

D. Long-range behavior of the nonrelativistic and relativistic potentials

When describing cold collisions between atoms it is crucial to ensure the proper long-range asymptotics of the interaction potential. The long-range coefficients describing the asymptotics of the nonrelativistic potentials are reported in Table III. An inspection of this Table shows that dispersion contribution C_6^{disp} is modest, but not negligible, of the order of 5% to 20%. The induction and dispersion coefficients are always positive, so they describe the attractive parts of the potentials. The electrostatic coefficients differ in sign depending on the state considered and are responsible for the appearance of barriers and long-range minima on the potential energy curves. This is illustrated on the left pannel of Fig. 8, where it is shown how the long-range asymptotics nicely fits the *ab initio* points. It is worth noting that the quadrupole moments are extremely sensitive to the electronic correlation. For instance, the value of C_3^{elst} for the $(3)^1\Sigma$ state is 1.16 at the LRCC3 level and 2.05 with the LRCCSD method. This means that the triple excitations diminish C_3^{elst} by as much as 44%. Surprisingly enough, such an effect is not observed for the hexadecapole moment. Here, the C_5^{elst} at the LRCC3 and LRCCSD differ by only 6%.

The long-range coefficients describing the large R asymptotics of the relativistic states are presented in Table IV. As discussed in III C in the atomic limit there is no spin-orbit coupling between the ground $X^1\Sigma$, $(1)^3\Sigma$, and $(2)^1\Sigma$ states with other states, so the long-range coefficients of the $(1)0^+$, $(1)1$, and $(2)0^+$ states remain unchanged in this approximation. An inspection of Table IV shows the SO coupling of the 3D and 1D states modestly affects the long-range coefficients in the $\text{Ba}({}^1D_2) + \text{Rb}^+({}^1S_0)$ dissociation limit. The SO coupling in the 3D multiplet introduces larger changes. For instance, the C_5^{elst} coefficient for the $(2)1$ state is zero. This is not fortuitous, but only reflects the fact that the hexadecapole moment of an atom in a 3D_1 state is identically zero. Again, the signs of the electrostatic coefficients are responsible for the barriers and long-range minima, cf. the right pannel of Fig. 8.

E. Elastic cross sections, spin-exchange, and radiative charge transfer

Thus far we have discussed the results of the electronic structure calculations. Now, we turn to the problem of sympathetic cooling of cold barium ions, and present the results for the elastic, spin-flip, and charge transfer cross sections for both the nonrelativistic and relativistic potentials. In Fig. 9 we report the elastic cross sections in the singlet and triplet manifolds, the spin-flip cross section, and the charge transfer cross section from the $(2)^1\Sigma$ to ground $X^1\Sigma$ state, all calculated from the nonrelativistic potentials. An inspection of this figure shows that in the ultracold regime the elastic cross sections behave according to the Wigner's threshold law, and the value of the cross section extrapolated to zero energy agrees very well with the one determined from the s wave scattering length. At energies around 100 nK the energy dependence of the cross sections starts to exhibit some structures related to shape resonances appearing due to the contributions of higher partial waves in the expansions (18) and to glory interference effects. Note that in the range of energies up to 1 mK the curves representing $\sigma_{\text{el}}^s(E)$ and $\sigma_{\text{el}}^t(E)$ are hardly distinguishable, despite the fact that the potential energy curves for the $(2)^1\Sigma$ and $(1)^3\Sigma$ states are quite different. This behavior is purely fortuitous, and is due to the fact that these two states have the same asymptotics and very close scattering lengths, a_s and a_t , equal to -3.53×10^5 and -4.26×10^5 Å, respectively. The superelastic spin-flip cross section shows a qualitatively similar behavior. Overall, all the elastic cross sections are very large, from around 10^{10} Å 2 at ultralow temperatures to $\approx 10^6$ Å 2 in the mK region.

In the ultacold regime the charge transfer cross section, which is an inelastic state changing cross section, decays as $E^{-1/2}$, in accordance with the Wigner's threshold law. At nanoKelvin temperatures this cross section, of the order of 10^4 Å 2 is five orders of magnitude smaller than the elastic cross sections. When we go up to the milliKelvin temperatures this ratio is even slightly more favorable, about five orders of magnitude of difference. Thus we can conclude that at the nonrelativistic level and with the single channel description of the collisional dynamics, cooling of the barium ion by collisions with ultracold rubidium atoms should be very efficient.

The results of dynamical calculations on the relativistic $(2)0^+$ and $(1)1$ potentials are presented on Fig. 10. The elastic cross section from the $(1)1$ state is almost identical to the cross section obtained with the nonrelativistic $(1)^3\Sigma$ potential. This is not surprising

since the spin-orbit coupling has a very small effect on the potential, slightly moving the repulsive wall, cf. Figs. 1 and 6. The relativistic scattering length is lower compared to the nonrelativistic $(1)^3\Sigma$ value, but most of the features, resonance structure and glory interference effects, are almost the same. By contrast, the energy dependence of the elastic cross section in the $(2)0^+$ potential is very different from that presented in Fig. 9 for the nonrelativistic potential. We note that the Wigner's limit is very different, and the resonant structure, glory ondulation, and all details at higher energies changed drastically. For instance, the scattering lengths for the $(2)0^+$ and $(1)1$ states are of -1.58×10^3 and -2.56×10^5 Å, to be compared with the values of a_s and a_t , -4.26×10^5 and -3.53×10^5 Å, quoted above. All these difference are not surprising, however, since the spin-orbit mixing has a profound effect in this case. In fact, up to $R \approx 15$ bohr, the point of the avoided crossing between the potential energy curves of the $(2)0^+$ and $(3)0^+$ states, the $(2)0^+$ potential has predominantly the character of the $(1)^3\Pi$ state. Only after the avoided crossing and mostly in the long range it becomes an almost pure $(2)^1\Sigma$ state. Also the spin-flip cross section computed from the relativistic potentials is quite different from the nonrelativistic one. It shows a sharp resonant structure around in the μK region.

The striking difference between the nonrelativistic and relativistic pictures is the fact that the charge transfer process is now allowed from both the $(2)0^+$ and $(1)1$ states. The corresponding cross sections as functions of the energy are also shown on Fig. 9. Again, we observe that the Wigner's threshold law with the $E^{-1/2}$ decay of the cross section in the ultracold regime is preserved. An inspection of this figure shows that the charge transfer process from the $(1)1$ state to the ground state will be very slow, unimportant at temperatures interesting from the experimental point of view. This is not a surprise, since the transition dipole moment from the $(1)1$ state to the ground state is very small, cf. Fig. 7. The charge transfer cross section from the $(2)0^+$ state is significantly larger, but again is several orders of magnitude smaller than the elastic one over all the range of temperatures considered in our work. In particular, in the milliKelvin regime, the inelastic events are six orders of magnitude less probable than the elastic. Thus, the relativistic calculations confirm the conclusions from the nonrelativistic case that the sympathetic cooling of the barium ion by collisions with ultracold rubidium atoms will be very efficient.

We would like to conclude this section by saying that the present single channel calculations strongly suggest that the sympathetic cooling of the barium atom by collisions

with ultracold rubidium atoms should be very efficient in the temperature range up to milliKelvin. The analysis presented here neglects the effect of the hyperfine splittings which are important at low collision energies. Thus, our single channel analysis performed in terms of singlet and triplet properties is only approximate at ultracold temperatures, and the actual collision rates will depend on the hyperfine spin states of the atom and ion. Moreover, other inelastic processes due to the presence of other channels could enter the game, and final conclusions can be presented only when full multichannel calculations are performed. Work in direction is in progress [53].

IV. SUMMARY AND CONCLUSIONS

In this paper we have reported theoretical prospects for the sympathetic cooling of the barium ion by collisions with the ultracold buffer gas of rubidium atoms. Potential energy curves for the ground $X^1\Sigma$ state of the $(\text{BaRb})^+$ molecular ion corresponding to the $\text{Rb}^+(^1\text{S}) + \text{Ba}(^1\text{S})$ dissociation and for the excited states, $(1)^3\Sigma$ and $(2)^1\Sigma$, corresponding to the $\text{Rb}(^2\text{S}) + \text{Ba}^+(^2\text{S})$ dissociation were computed by means of size-consistent coupled cluster methods with single, double, and triple excitations in the wave function. The inclusion of the triple excitations in the wave function was shown to be essential for the open-shell $(2)^1\Sigma$ state. The $(\text{BaRb})^+$ molecular ion shows a lot of low-lying molecular states, and the corresponding potential energy curves were computed as well. Using the molecular spin-orbit coupling matrix elements relativistic potential energy curves were obtained. The asymptotics of the nonrelativistic and relativistic potentials was fixed with long-range coefficients calculated from C_3 up to and including C_6 . A good understanding of the dynamics in the $(\text{BaRb})^+$ system requires the knowledge of the nonadiabatic (radial and angular) coupling matrix elements, which were calculated as well. Finally, the electric dipole transition moments from the ground state were computed. Based on the above *ab initio* electronic structure calculations, single channel dynamical calculations of the elastic, spin-exchange, and inelastic cross sections for the collisions of the $\text{Ba}^+(^2\text{S})$ ion with the $\text{Rb}(^2\text{S})$ in the energy range from 0 to 1 mK were performed, using both the nonrelativistic and relativistic potentials. It was found that the elastic processes are a few orders of magnitude more favorable than the inelastic ones. Thus, we can conclude our paper by saying that the sympathetic cooling of the barium ion by the buffer gas of ultracold rubidium atoms should be very

efficient taking into account the two-body collisional properties of Rb and Ba⁺.

Acknowledgments

We would like to thank Agnieszka Witkowska for fruitful discussions, and for reading and commenting on the manuscript. This work was supported by the Polish Ministry of Science and Higher Education (grants 1165/ESF/2007/03 and PBZ/MNiSW/07/2006/41), and the Foundation for Polish Science (FNP) via Homing program (grant no. HOM/2008/10B) within the EEA Financial Mechanism.

- [1] A. T. Grier, M. Cetina, F. Oruevi, and V. Vuleti, Phys. Rev. Lett. **102**, 223201 (2009).
- [2] W. W. Smith, O. P. Makarov, and J. Lin, J. Mod. Opt. 52, 2253 (2005).
- [3] C. Zipkes, S. Palzer, C. Sias, and M. Köhl, Nature **464**, 388 (2010).
- [4] C. Zipkes, S. Palzer, L. Ratschbacher, C. Sias, M. Köhl, arXiv:1005.3846.
- [5] S. Schmid, A. Härter and J.H. Denschlag, arXiv:1007.4717.
- [6] R. Côté and A. Dalgarno, Phys. Rev. A **62**, 012709 (2000).
- [7] E. Bodo, P. Zhang, and A. Dalgarno, New J. Phys. **10**, 033024 (2008).
- [8] Z. Idziaszek, T. Calarco, P. S. Julienne, and A. Simoni, Phys. Rev. A 79, 010702(R) (2009).
- [9] Z. Idziaszek, T. Calarco, and P. Zoller, Phys. Rev. A **76**, 033409 (16) (2007).
- [10] H. Doerk, Z. Idziaszek, and T. Calarco, Phys. Rev. A **81**, 012708 (2010).
- [11] P. Massignan, C. J. Pethick, and H. Smith, Phys. Rev. A **71**, 023606 (2005).
- [12] R. Côté, V. Kharchenko, and M. D. Lukin, Phys. Rev. Lett. **89**, 093001 (2002).
- [13] O.P. Makarov, R. Côté, H. Michels, and W.W. Smith, Phys. Rev. A **67**, 042705 (2003).
- [14] B. Bussery-Honvault, J.-M. Launay, and R. Moszynski, Phys. Rev. A **68**, 032718 (2003).
- [15] B. Bussery-Honvault, J.-M. Launay, and R. Moszynski, Phys. Rev. A **72**, 012702 (2005).
- [16] B. Bussery-Honvault, J.-M. Launay, T. Korona, and R. Moszynski, J. Chem. Phys. **125**, 114315 (2006).
- [17] B. Bussery-Honvault and R. Moszynski, Mol. Phys. **104**, 2387 (2006).
- [18] C.P. Koch and R. Moszynski, Phys. Rev. A **78**, 043417 (2008).
- [19] S. Knecht, H.J.Aa. Jensen, and T. Fleig, J. Chem. Phys. **128**, 014108 (2008).
- [20] S. Knecht, L.K. Sørensen, H.J.Aa. Jensen, T. Fleig, and C.M. Marian, J. Phys. B **43**, 055101 (2010).
- [21] H. Koch and P. Jørgensen, J. Chem. Phys. **93**, 3333 (1990).
- [22] H. Koch, O. Christiansen, P. Jørgensen, A. Sanchez de Meras, And T. Helgaker, J. Chem. Phys. **106**, 1808 (1997).
- [23] B. Jeziorski, Mol. Phys. – in press.
- [24] T. Helgaker, H. J. Aa. Jensen, P. Jørgensen, J. Olsen, K. Ruud, H. Ågren, A. A. Auer, K. L. Bak, V. Bakken, O. Christiansen, S. Coriani, P. Dahle, E. K. Dalskov, T. Enevoldsen, B. Fernandez, C. Hättig, K. Hald, A. Halkier, H. Heiberg, H. Hettema, D. Jonsson, S. Kirpekar,

R. Kobayashi, H. Koch, K. V. Mikkelsen, P. Norman, M. J. Packer, T. B. Pedersen, T. A. Ruden, A. Sanchez, T. Saue, S. P. A. Sauer, B. Schimmelpfenning, K. O. Sylvester-Hvid, P. R. Taylor, O. Vahtras, DALTON, an *ab initio* electronic structure program, Release 1.2 (2001).

[25] MOLPRO is a package of *ab initio* programs written by H.-J. Werner and P. J. Knowles, with contributions from R. D. Amos, A. Bernhardsson, A. Berning, P. Celani, D. L. Cooper, M. J. O. Deegan, A. J. Dobbyn, F. Eckert, C. Hampel, G. Hetzer, T. Korona, R. Lindh, A. W. Lloyd, S. J. McNicholas, F. R. Manby, W. Meyer, M. E. Mura, A. Nicklass, P. Palmieri, R. Pitzer, G. Rauhut, M. Schütz, H. Stoll, A. J. Stone, R. Tarroni, and T. Thorsteinsson.

[26] O. Christiansen, A. Halkier, H. Koch, P. Jørgensen, and T. Helgaker, *J. Chem. Phys.* **108**, 2801 (1998).

[27] P.R. Bunker and P. Jensen, *Molecular Symmetry and Spectroscopy*, (NRC Press, Ottawa, 1998).

[28] B. Jeziorski, R. Moszynski, and K. Szalewicz, *Chem. Rev.* **94**, 1887 (1994).

[29] R. Moszynski, in: *Molecular Materials with Specific Interactions – Modeling and Design*, edited by W.A. Sokalski, (Springer, New York, 2007), pp. 1–157.

[30] B. Jeziorski and R. Moszynski, *Int. J. Quantum Chem.* **48**, 161 (1993).

[31] R. Moszynski, P.S. Zuchowski, and B. Jeziorski *Collect. Czech. Chem. Comun.* **70**, 1109 (2005).

[32] T. Korona, M. Przybytek, and B. Jeziorski, *Mol. Phys.* **104**, 2303 (2006).

[33] K.D. Bonin and V.V. Kresnin, *Electric dipole polarizabilities of atoms, molecules, and clusters*, (Eorld Scientific, New York, 1997), pp. 36-38.

[34] W. Skomorowski, R. Moszynski, and K. Pachucki, to be published.

[35] A. Derevianko, S.G. Porsev, and J.F. Babb, *At. Data Nucl. Data Tables* **96**, 323 (2010).

[36] H.A. Bethe and E.E. Salpeter, *Quantum Mechanics of One- and Two-Electron Atoms*, (Academic Press, New York, 1957), p. 170.

[37] A. Dalgarno and M.R.H. Rudge, *Proc. Royal Soc. (London)A* **286**, 519 (1965).

[38] H. T. C. Stoof, J. M. V. A. Koelman, and B. J. Verhaar, *Phys. Rev. B* **38**, 4688 (1988).

[39] E. Timmermans and R. Côté, *Phys. Rev. Lett.* **80**, 3419 (1998).

[40] B. Zygelman and A. Dalgarno, *Phys. Rev. A* **38**, 1877 (1988).

[41] J. Tellinghuisen and P.S. Julienne, *J. Chem. Phys.* **81**, 5779 (1984).

[42] <http://physics.nist.gov/PhysRefData/Handbook/Tables/bariumtable5.htm>

- [43] W. Skomorowski and R. Moszynski, to be published.
- [44] I.S. Lim, H. Stoll, P. Schwerdtfeger, J. Chem. Phys. **124**, 034107 (2006).
- [45] I.S. Lim, P. Schwerdtfeger, B. Metz, H. Stoll, J. Chem. Phys. **122**, 104103 (2005).
- [46] J. Brown and A. Carrington, *Rotational spectroscopy of diatomic molecules*, (Cambridge University Press, Cambridge, 2003), pp. 225–229.
- [47] S. F. Boys and F. Bernardi, Mol. Phys. **19**, 553 (1970).
- [48] H.L. Schwartz, T.M. Miller, and B. Bederson, Phys. Rev. A **10**, 1924 (1974).
- [49] E. Iskrenova-Tchoukova and M.S. Safronova, Phys. Rev. A **78**, 012508 (2008).
- [50] B. K. Sahoo, R.G.E. Timmermans, B.P. Das, and D. Mukherjee, Phys. Rev. A **80**, 062506 (2009).
- [51] E.L. Snow and S.R. Lundeen, Phys. Rev. A **76**, 052505 (2007).
- [52] M.G. Kozlov and S.G. Porsev, European Phys. J. D **5**, 59 (1999).
- [53] A. Simoni et al., to be published.

TABLE I: Spectroscopic characteristics of the nonrelativistic electronic states of the $(\text{BaRb})^+$ molecular ion.

State	R_e (bohr)	D_e (cm^{-1})	T_e (cm^{-1})	Reference	Dissociation
$\text{X}^1\Sigma$	8.67	5136	0	present	$\text{Ba}(^1\text{S})+\text{Rb}^+(^1\text{S})$
	8.85		0	Ref. [19]	
$(1)^3\Sigma$	9.27	6587	6893	present	$\text{Ba}^+(^2\text{S})+\text{Rb}(^2\text{S})$
	9.38		6808	Ref. [19]	
$(2)^1\Sigma$ (primary minimum)	9.02	911	12569	present	$\text{Ba}^+(^2\text{S})+\text{Rb}(^2\text{S})$
$(2)^1\Sigma$ (secondary minimum)	15.19	576	12904	present	$\text{Ba}^+(^2\text{S})+\text{Rb}(^2\text{S})$
$(2)^3\Sigma$ (primary minimum)	9.82	1874	12683	present	$\text{Ba}(^3\text{D})+\text{Rb}^+(^1\text{S})$
	9.58		13478	Ref. [19]	
$(2)^3\Sigma$ (secondary minimum)	16.78	697	13861	present	$\text{Ba}(^3\text{D})+\text{Rb}^+(^1\text{S})$
$(1)^3\Pi$	8.19	6301	8257	present	$\text{Ba}(^3\text{D})+\text{Rb}^+(^1\text{S})$
	8.17		8832	Ref. [19]	
$(1)^3\Delta$	9.11	4380	10178	present	$\text{Ba}(^3\text{D})+\text{Rb}^+(^1\text{S})$
	9.19		10776	Ref. [19]	
$(3)^1\Sigma$	12.00	1858	15146	present	$\text{Ba}(^1\text{D})+\text{Rb}^+(^1\text{S})$
$(1)^1\Pi$	9.04	4403	12601	present	$\text{Ba}(^1\text{D})+\text{Rb}^+(^1\text{S})$
	8.44		15906	Ref. [19]	
$(1)^1\Delta$	9.08	5769	11236	present	$\text{Ba}(^1\text{D})+\text{Rb}^+(^1\text{S})$
	9.19		11276	Ref. [19]	

TABLE II: Spectroscopic characteristics of the relativistic electronic states of the $(\text{BaRb})^+$ molecular ion.

State	R_e (bohr)	D_e (cm $^{-1}$)	T_e (cm $^{-1}$)	Reference	Dissociation
(1)0 $^+$	8.67	5136	0	present	$\text{Ba}(^1\text{S}_0) + \text{Rb}^+(^1\text{S}_0)$
	8.72	5055	0	Ref. [20]	
(1)1	9.25	6609	6872	present	$\text{Ba}^+(^2\text{S}_{1/2}) + \text{Rb}(^2\text{S}_{1/2})$
	9.22	6871	6638	Ref. [20]	
(2)0 $^+$	8.17	5403	8077	present	$\text{Ba}^+(^2\text{S}_{1/2}) + \text{Rb}(^2\text{S}_{1/2})$
	8.28	5899	7775	Ref. [20]	
(2)1	8.27	5878	8293	present	$\text{Ba}(^3\text{D}_1) + \text{Rb}^+(^1\text{S}_0)$
	8.28	5742	7932	Ref. [20]	
(3)1	9.10	4497	9893	present	$\text{Ba}(^3\text{D}_2) + \text{Rb}^+(^1\text{S}_0)$
	9.22	4302	9556	Ref. [20]	
(4)1	9.41	2353	12464	present	$\text{Ba}(^3\text{D}_3) + \text{Rb}^+(^1\text{S}_0)$
	9.22	2258	11963	Ref. [20]	
(3)0 $^+$	9.01	1801	12589	present	$\text{Ba}(^3\text{D}_2) + \text{Rb}^+(^1\text{S}_0)$
	9.03		12005	Ref. [20]	
(5)1	9.45	4108	12936	present	$\text{Ba}(^1\text{D}_2) + \text{Rb}^+(^1\text{S}_0)$
	9.72	3556	12687	Ref. [20]	
(4)0 $^+$	12.01	1890	15153	present	$\text{Ba}(^1\text{D}_2) + \text{Rb}^+(^1\text{S}_0)$

TABLE III: Long-range coefficients (in atomic units) for the nonrelativistic electronic states of the $(\text{BaRb})^+$ molecular ion. C_6 is the sum $C_6^{\text{ind}} + C_6^{\text{disp}}$.

State	C_3^{elst}	C_4^{ind}	C_5^{elst}	C_6^{ind}	C_6^{disp}	C_6	Dissociation
$X^1\Sigma$		136.8		4450	368	4818	$\text{Ba}(^1\text{S}) + \text{Rb}^+(^1\text{S})$
$(1)^3\Sigma$		159.3		3260	2510	5770	$\text{Ba}^+(^2\text{S}) + \text{Rb}(^2\text{S})$
$(2)^1\Sigma$		159.3		3260	2510	5770	$\text{Ba}^+(^2\text{S}) + \text{Rb}(^2\text{S})$
$(2)^3\Sigma$	-4.55	324.1	106.3	1873	392	2265	$\text{Ba}(^3\text{D}) + \text{Rb}^+(^1\text{S})$
$(1)^3\Pi$	-2.27	272.0	-71.0	2718	372	3090	$\text{Ba}(^3\text{D}) + \text{Rb}^+(^1\text{S})$
$(1)^3\Delta$	4.55	115.1	18.1	3060	322	3382	$\text{Ba}(^3\text{D}) + \text{Rb}^+(^1\text{S})$
$(3)^1\Sigma$	-1.16	108.1	154.3	2844	661	3505	$\text{Ba}(^1\text{D}) + \text{Rb}^+(^1\text{S})$
$(1)^1\Pi$	-0.58	127.0	-102.9	2878	244	3122	$\text{Ba}(^1\text{D}) + \text{Rb}^+(^1\text{S})$
$(1)^1\Delta$	1.16	180.9	25.7	3802	273	4075	$\text{Ba}(^1\text{D}) + \text{Rb}^+(^1\text{S})$

TABLE IV: Long-range coefficients (in atomic units) for the relativistic electronic states of the $(\text{BaRb})^+$ molecular ion.

State	C_3^{elst}	C_4^{ind}	C_5^{elst}	C_6	Dissociation
(1)0 ⁺		136.8		4818	$\text{Ba}(^1\text{S}_0) + \text{Rb}^+(^1\text{S}_0)$
(1)1		159.3		5770	$\text{Ba}^+(^2\text{S}_{1/2}) + \text{Rb}(^2\text{S}_{1/2})$
(2)0 ⁺		159.3		5770	$\text{Ba}^+(^2\text{S}_{1/2}) + \text{Rb}(^2\text{S}_{1/2})$
(2)1	1.60	183.0	0.0	3183	$\text{Ba}(^3\text{D}_1) + \text{Rb}^+(^1\text{S}_0)$
(3)1	-1.13	244.0	46.0	2780	$\text{Ba}(^3\text{D}_2) + \text{Rb}^+(^1\text{S}_0)$
(4)1	-2.73	282.0	6.0	3382	$\text{Ba}(^3\text{D}_3) + \text{Rb}^+(^1\text{S}_0)$
(3)0 ⁺	-2.25	270.0	-66.7	3096	$\text{Ba}(^3\text{D}_2) + \text{Rb}^+(^1\text{S}_0)$
(5)1	-0.59	129.0	-101.0	3117	$\text{Ba}(^1\text{D}_2) + \text{Rb}^+(^1\text{S}_0)$
(4)0 ⁺	-1.18	110.0	151.0	3493	$\text{Ba}(^1\text{D}_2) + \text{Rb}^+(^1\text{S}_0)$

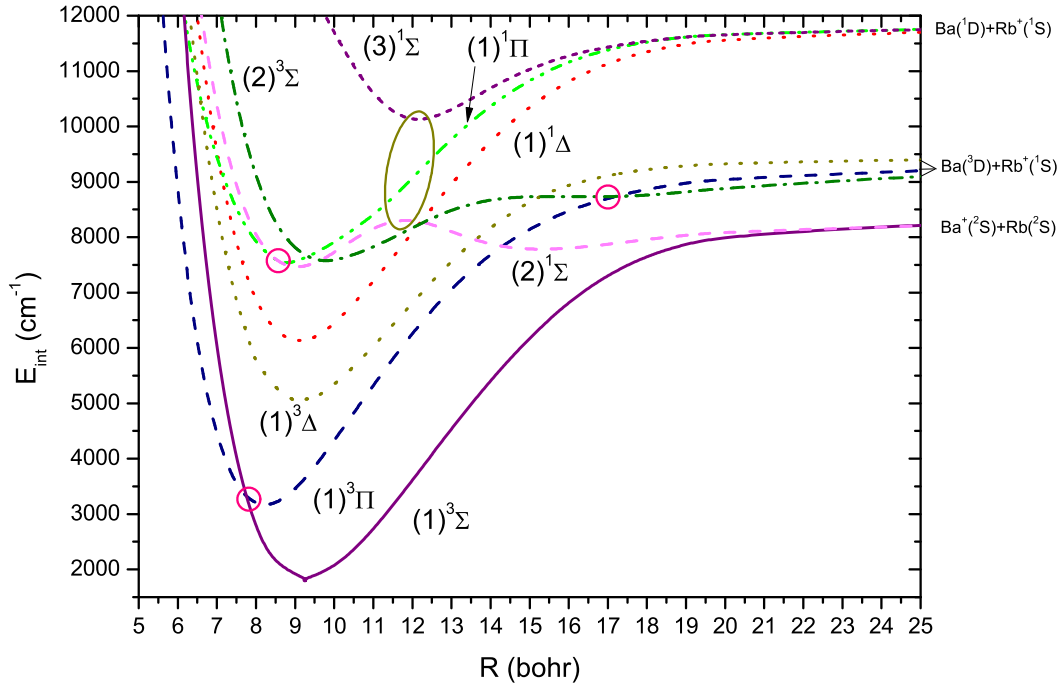


FIG. 1: Nonrelativistic potential energy curves for the excited states of the $(\text{BaRb})^+$ molecular ion.

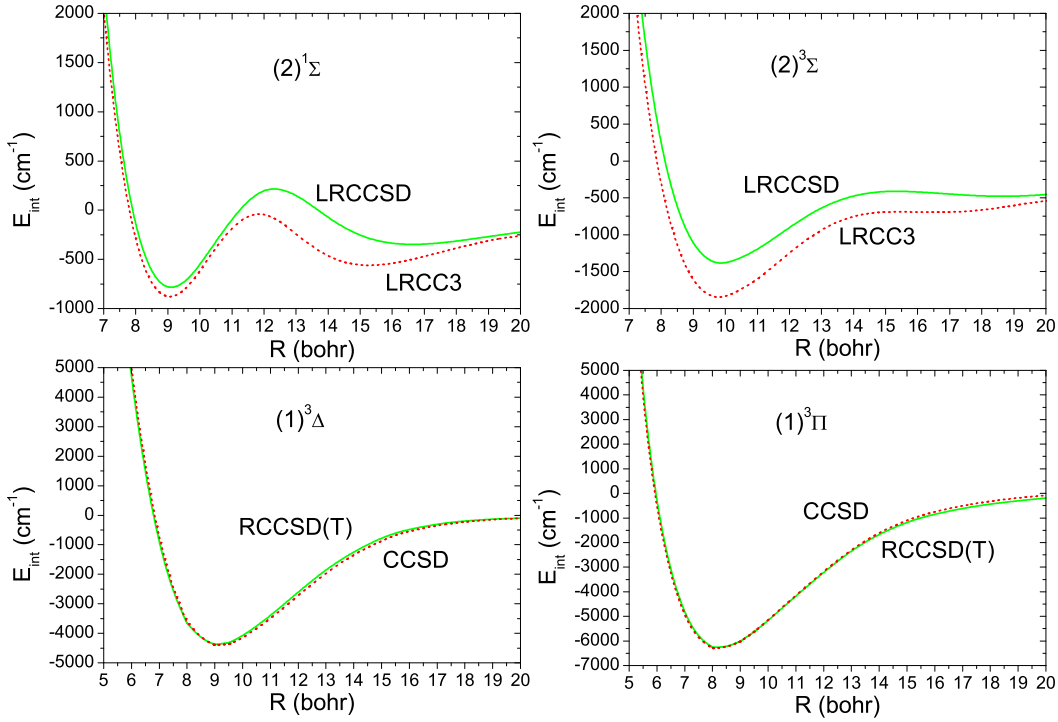


FIG. 2: Comparison of the LRCC3 with CCSD, and RCCSD(T) with LRCCSD potential energy curves for selected states of the $(\text{BaRb})^+$ molecular ion.

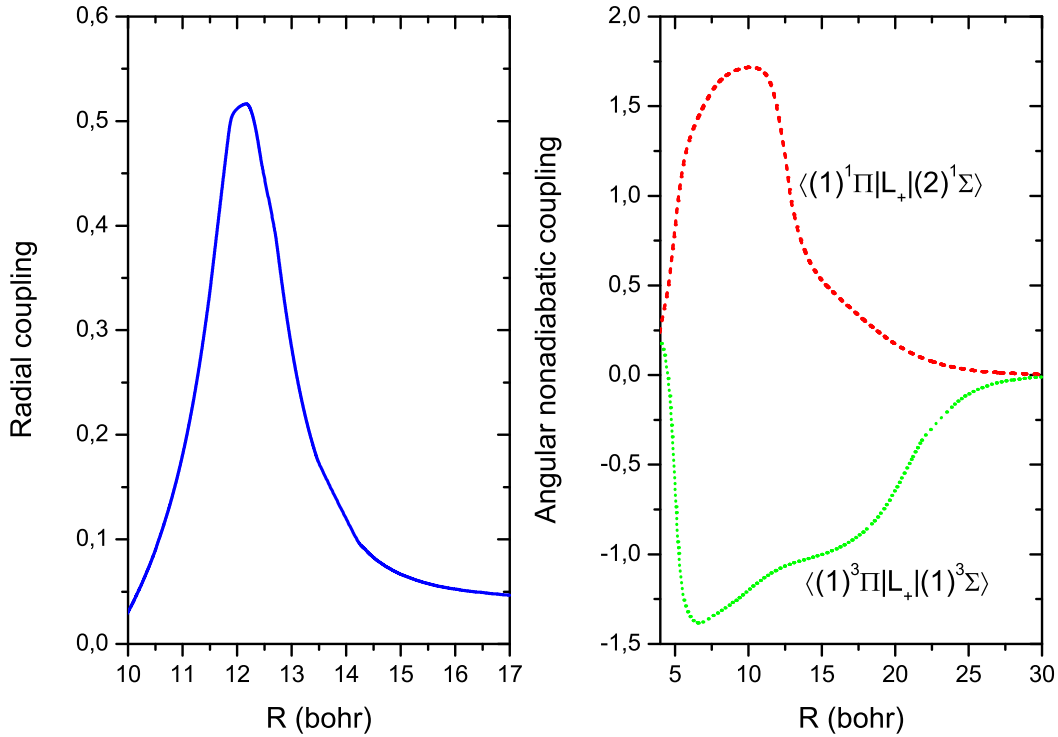


FIG. 3: Nonadiabatic coupling matrix elements of the nonrelativistic electronic states of the $(\text{BaRb})^+$ molecular ion. The left and right panels correspond to the radial and angular couplings, respectively.

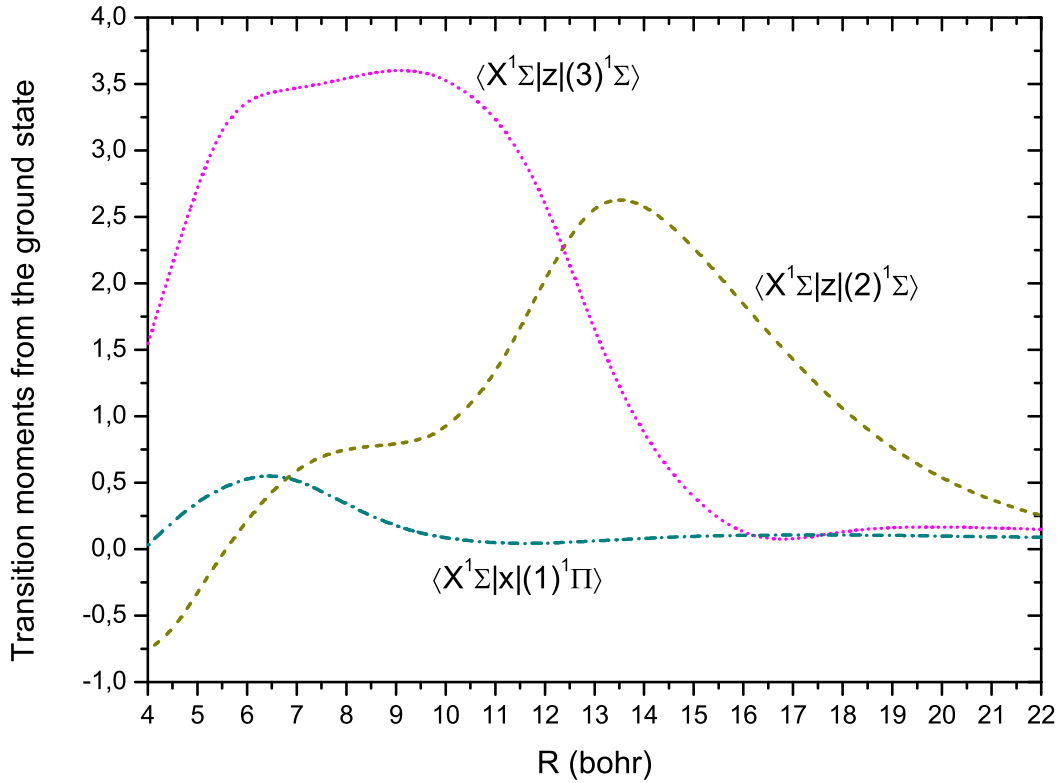


FIG. 4: Electric transition dipole moments from the ground $X^1\Sigma$ state to the ${}^1\Sigma$ and ${}^1\Pi$ states of $(\text{BaRb})^+$.

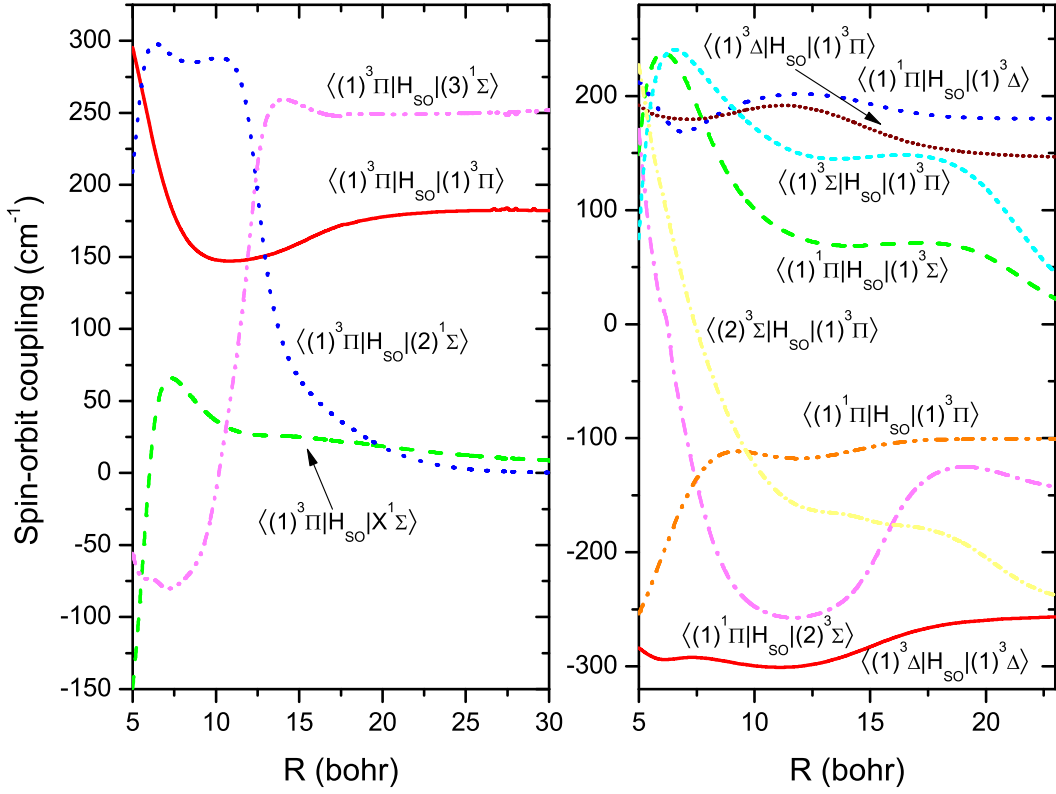


FIG. 5: Matrix elements of the spin-orbit coupling for the electronic states of $(\text{BaRb})^+$. The left and right panels correspond to 0^+ and 1 states, respectively.

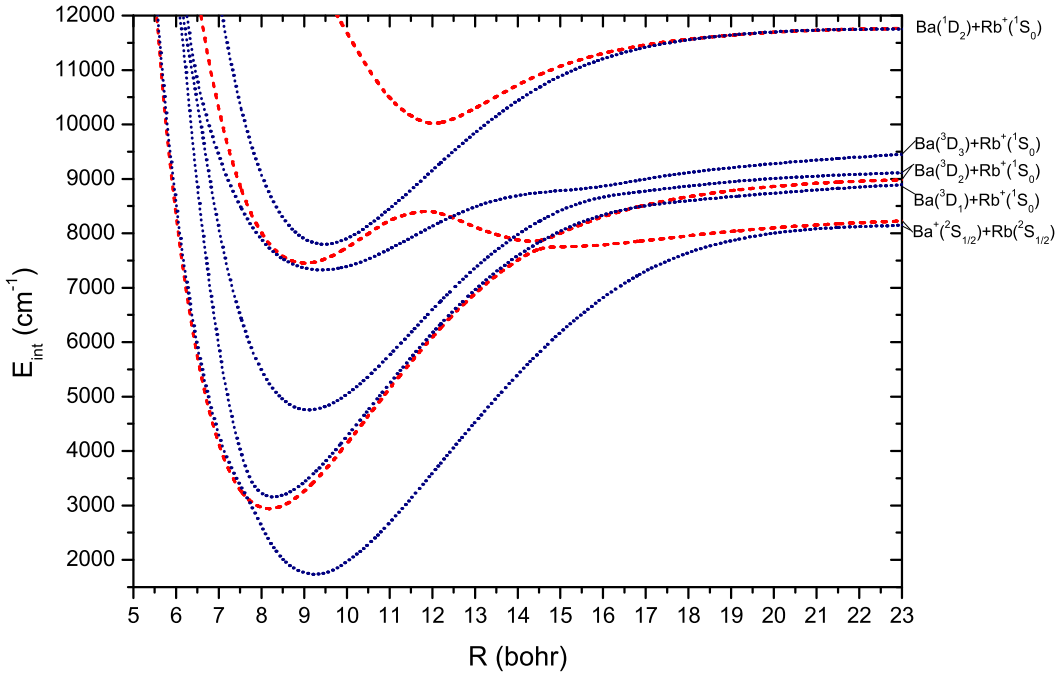


FIG. 6: Relativistic potential energy curves for the excited states of the $(\text{BaRb})^+$ molecular ion. Red dashed lines correspond to the 0^+ states and the blue dotted lines to the 1^+ states.

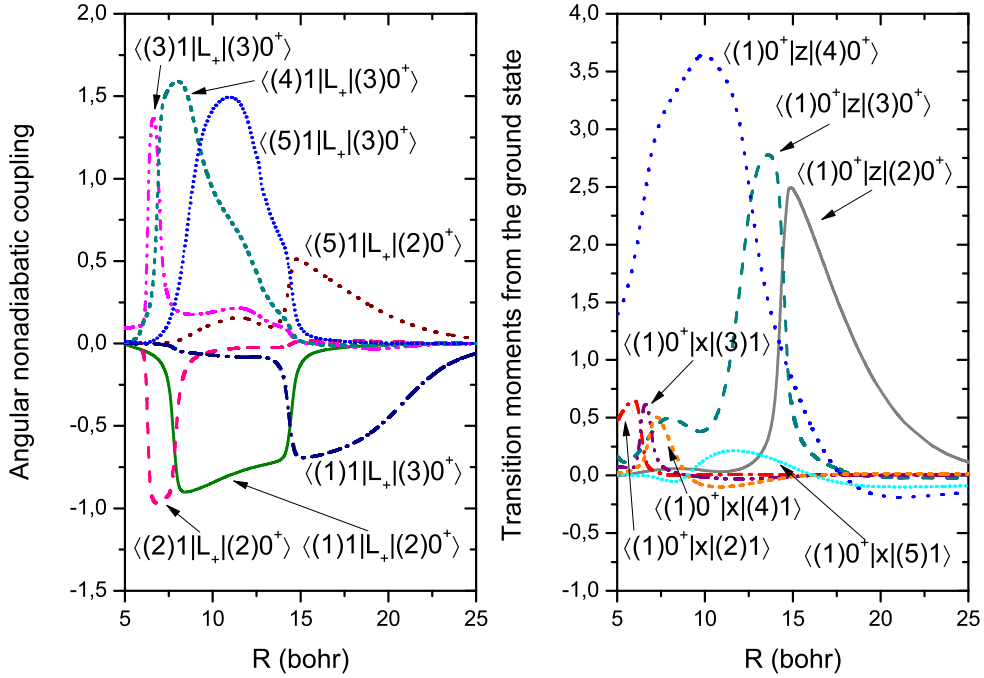


FIG. 7: Nonadiabatic coupling matrix elements of the relativistic electronic states and relativistic electric transition dipole moments of the $(\text{BaRb})^+$ molecular ion. The left and right pannels correspond to the nonadiabatic couplings and transition moments, respectively.

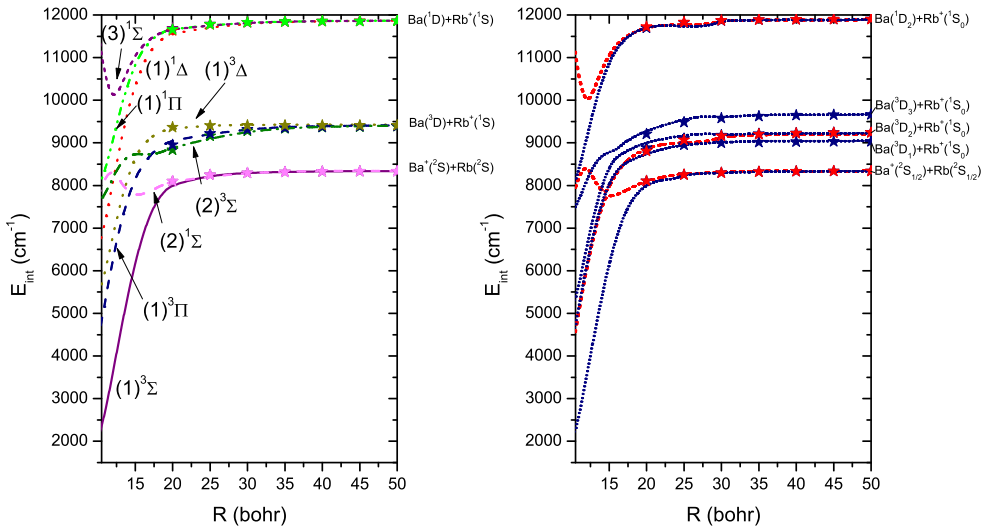


FIG. 8: Long range nonrelativistic (left pannel) and relativistic (right pannel) potential energy curves of the $(\text{BaRb})^+$ molecular ion. Stars are based on long range coefficients like in Eq. 3.

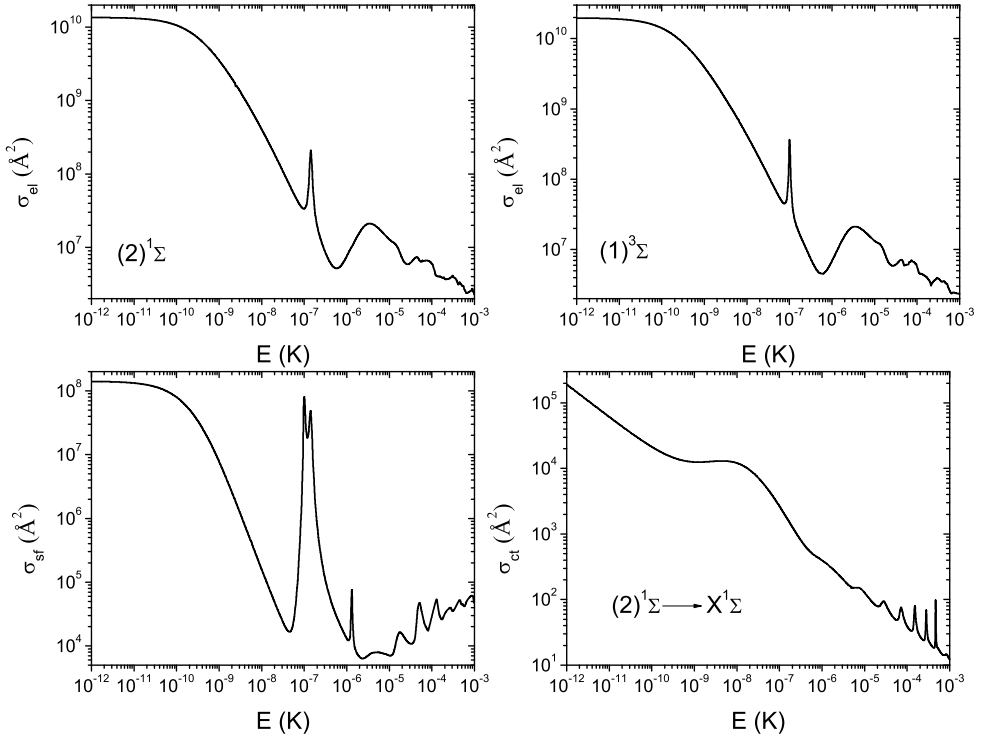


FIG. 9: Elastic, spin-flip, and charge transfer cross sections for collisions of $^{138}\text{Ba}^+(^2\text{S})$ and $^{87}\text{Rb}(^2\text{S})$ as functions of the collision energy from nonrelativistic potentials.

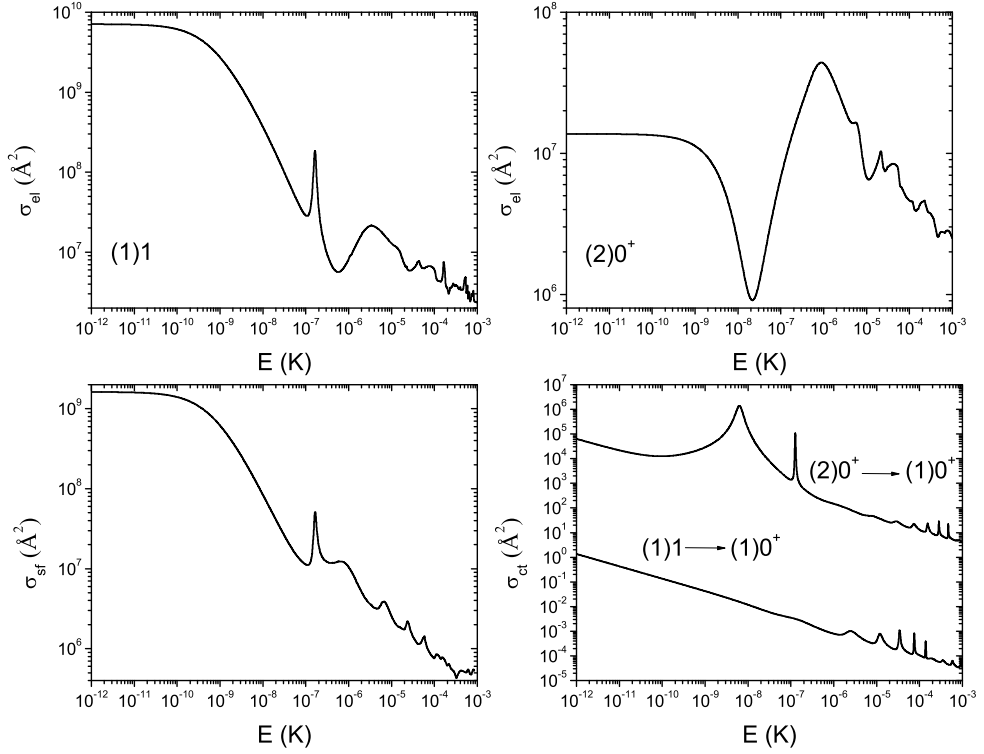


FIG. 10: Elastic, spin-flip, and charge transfer cross sections for collisions of $^{138}\text{Ba}^+(2\text{S})$ and $^{87}\text{Rb}(2\text{S})$ as functions of the collision energy from relativistic potentials.